Heliyon

ELSEVIER

Received:
4 December 2018
Revised:
19 January 2019
Accepted:
7 February 2019

Cite as: Pınar Acar. Multi-scale computational modeling of lightweight aluminum-lithium alloys. Heliyon 5 (2019) e01225. doi: 10.1016/j.heliyon.2019.e01225

Multi-scale computational modeling of lightweight aluminum-lithium alloys

Pınar Acar *

Virginia Tech, Blacksburg, 24061, VA, USA

* Corresponding author.
E-mail address: pacar@vt.edu.

Abstract

The present study addresses the multi-scale computational modeling of a lightweight Aluminum-Lithium (Al-Li) 2070 alloy. The Al-Li alloys display significant anisotropy in material properties because of their strong crystallographic texture. To understand the relationships between processing, microstructural textures at different material points and tailored material properties, a multi-scale simulation is performed by controlling the texture evolution during deformation. To achieve the multi-scale framework, a crystal plasticity model based on a one-point probability descriptor, Orientation Distribution Function (ODF), is implemented to study the texture evolution. Next, a two-way coupled multi-scale model is developed, where the deformation gradient at the macro-scale integration points is passed to the micro-scale ODF model and the homogenized stress tensor at the micro-scale is passed back to the macro-scale model. A gradient-based optimization scheme which incorporates the multi-scale continuum sensitivity method is utilized to calibrate the slip system parameters of the alloy using the available experimental data. Next, the multi-scale simulations are performed for compression and tension using the calibrated crystal plasticity model, and the texture data is compared to the experiments. With the presented multi-scale modeling scheme, we achieve the location-specific texture predictions for a new generation Al-Li alloy for different deformation processes.

Keywords: Materials science

https://doi.org/10.1016/j.heliyon.2019.e01225

1. Introduction

The new-generation Aluminum-Lithium (Al-Li) alloys are attractive materials especially for the aircraft industry owing to their low weights. However, these alloys demonstrate a significant anisotropy [1, 2] on material properties, which primarily stems from the crystallographic texture formation during deformation processing [3, 4]. Therefore, the texture formation can be studied to achieve the optimized directional material properties and underlying microstructure designs by controlling the deformation processing. Instead of the traditional trial-error approach in materials design, we are now moving towards a new era of computational design under the Integrated Computational Materials Engineering (ICME) paradigm. This paradigm leads to the coupling of engineering finite element (FE) techniques with microstructural models to compute the evolution of the microstructure during deformation. Therefore, ICME encourages the use of computational models to investigate the effects of different process parameters (preform shape, forging velocity, die shape) on the microstructure [5] to achieve location-specific material properties. The location-specific texture and material properties can also be predicted in metal forming processes for a specimen that is subjected to different deformation histories at different locations. There is a two-coupling between the micro and macro scales. The two-way coupling ensures that effect of texture-dependent properties is adequately taken into account during deformation. A better understanding of the evolution of crystallographic texture and material anisotropy during processing would be possible utilizing experimental and computational data together. In case of Al-Li alloys, understanding the micro-mechanisms in texture development is important for finding optimized directional material properties. Studying the texture evolution of Al-Li alloys is also of interest in this work.

The texture evolution and mechanical response of polycrystalline materials at the micro-scale can be analyzed with crystal plasticity (CP) [6, 7, 8, 9, 10], which leads to the modeling for the micro-mechanisms of plastic deformation using elasto-viscoplastic constitutive laws [11] for various slip systems. With the CP computational models, the texture evolution and the mechanical response of the material during deformation can be simulated using parameters such as slip system strengths and hardening rates. One traditional approach to analyze the CP behavior of polycrystalline materials is to utilize crystal plasticity finite element (CPFE) models. However, the CPFE models are computationally expensive and they are not well-suited for modeling of the two-way micro-macro coupling to achieve multi-scale simulations. Therefore, in the present study, we develop a reduced-order modeling approach based on a probabilistic texture descriptor, Orientation Distribution Function (ODF), to predict the texture evolution at different material points. In this method, the polycrystalline microstructure is represented using an

 https://doi.org/10.1016/j.heliyon.2019.e01225

FE discretization of the continuous orientation space, and the texture evolution is controlled through the ODF conservation laws.

The main goal of this study is to achieve a multi-scale computational model for the Al-Li 2070 alloy. To perform the multi-scale simulation, we need the slip system parameters of the alloy to utilize the CP models. The slip system parameters of the lightweight Al-Li 2070 alloy are not openly available in the literature. Therefore, the slip system parameters of the alloy are identified by performing an optimization on the multi-scale computational model to minimize the difference between the simulation outputs and the available experimental data for the Al-Li 2070 alloy in the literature [12, 13]. This leads to an inverse problem that is solved with a gradient-based optimization strategy utilizing sensitivities computed with multi-scale continuum sensitivity method (MCSM) [5]. After the identification of the slip system parameters, the multi-scale simulation is conducted to predict the texture evolution and corresponding material property distribution of the Al-Li 2070 alloy. The microstructural texture is quantified by the ODF values, and the texture evolution is controlled with the ODF conservation laws. The ODF approach has been previously studied by the author for microstructure design optimization of different polycrystalline materials, such as α-Titanium [14, 15, 16, 17] and Galfenol [15, 18]. However, the previous effort in the field concentrated on the modeling of the microstructure at one material control point rather than utilizing a multi-scale modeling approach that works coupled with micro-scale simulations at various material points. In contrast to the previous efforts, in this work, we address the multi-scale modeling of lightweight Al-Li 2070 alloy in a forming deformation process to predict the slip system parameters and microstructural texture evolution of the material. Therefore, the findings of this study will lead to a preliminary step towards the ICME goals for achieving the multi-scale design of deformation processes and microstructures to obtain optimum directional material properties. The organization of the paper is as follows. The ODF based texture evolution model, elasto-viscoplastic single crystal model, and the computational model for the forming deformation process are explained in Section 2. The slip system parameters identification and the multi-scale simulation of Al-Li 2070 alloy are discussed in Section 3. The conclusions and the potential extensions as a future work are addressed in Section 4.

2. Background

This section addresses the modeling of microstructural evolution with the ODF approach, elasto-viscoplastic single crystal constitutive model and the computational model for the forming simulation.

 https://doi.org/10.1016/j.heliyon.2019.e01225

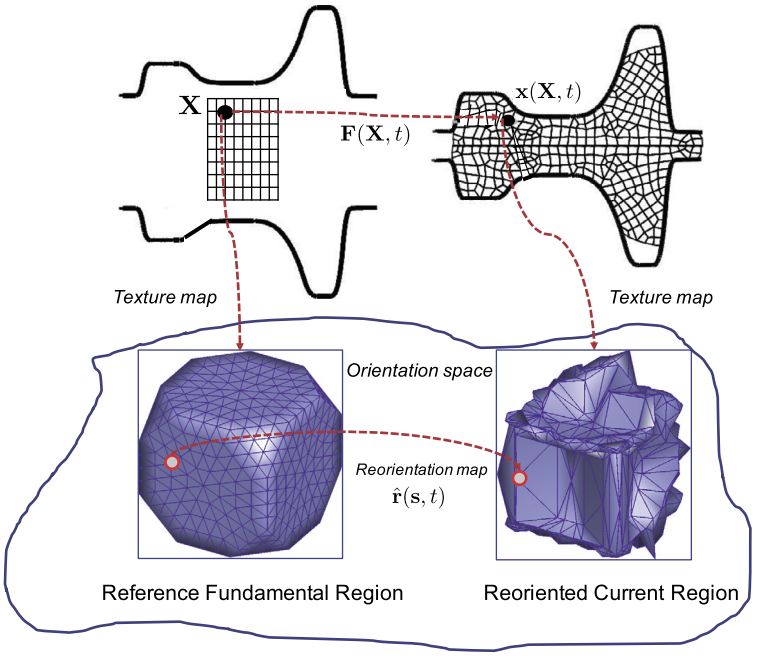

Figure 1. The texture evolution at a material point, X, is represented with a Lagrangian framework using parameters, $\boldsymbol{s}$ and $\boldsymbol{r}$, selected within the reference fundamental region.

2.1. Microstructural evolution with the ODF

The polycrystalline material can be modeled in the fundamental region using the crystallographic symmetries rather than the entire orientation space. The crystal orientation can be defined in terms of a coordinate $\boldsymbol{r}$, which can be obtained through parameterization. In this work, we use the Rodrigues-Frank (RF) vector for parameterization of the crystal orientation and the texture is quantified using the ODF, $\boldsymbol{A}$. The texture evolution is described using a re-orientation vector $\hat{\boldsymbol{r}}(\boldsymbol{s}, t)$, which maps the location $\boldsymbol{r}$ in the reoriented region (at time t) to the corresponding location $\boldsymbol{s}$ in the reference fundamental region (at time $t = 0$) as shown in Figure 1. The ODF can be studied using the Eulerian ($\boldsymbol{A}(\boldsymbol{r}, t)$) or Lagrangian ($\hat{\boldsymbol{A}}(\boldsymbol{s}, t)$) representations, which are related with Eq. (1):

$$\boldsymbol{A}(\boldsymbol{r}, t) = \boldsymbol{A}(\hat{\boldsymbol{r}}(\boldsymbol{s}, t), t) = \hat{\boldsymbol{A}}(\boldsymbol{s}, t) \tag{1}$$

In this work, the ODF conservation equation is utilized to obtain the ODF at time, t, using the Lagrangian representation with Eq. (2):

$$\hat{\boldsymbol{A}}(\boldsymbol{s}, t)\boldsymbol{J}(\boldsymbol{s}, t) = \hat{\boldsymbol{A}}(\boldsymbol{s}, 0) = \boldsymbol{A_0}(\boldsymbol{s}) \tag{2}$$

where $\boldsymbol{J}(\boldsymbol{s}, t) = det(\nabla\hat{\boldsymbol{r}}(\boldsymbol{s}, t))$ is the Jacobian determinant of the re-orientation of crystals and $\hat{\boldsymbol{A}}(\boldsymbol{s}, 0) = \boldsymbol{A_0}(\boldsymbol{s})$ is the initial texture of the material. The physical explanation of the conservation law in Eq. (2) can be found in other references

 https://doi.org/10.1016/j.heliyon.2019.e01225

[19, 20, 21] and is not repeated for brevity. The ODF is discretized on the RF fundamental region using an FE mesh. The RF approach provides an angle-axis type of unique representation of the orientation using a rotation axis $\boldsymbol{n}$ and an angle of rotation ϕ about this axis. The RF parameters are solved by scaling the axis of rotation as shown in Eq. (3):

$$\boldsymbol{r} = \boldsymbol{n} \tan \frac{\phi}{2} \tag{3}$$

The relation between the orientation, $\boldsymbol{r}$, and the rotation, $\boldsymbol{R}$, is represented by Eq. (4):

$$\boldsymbol{R} = \frac{1}{1 + \boldsymbol{r} \cdot \boldsymbol{r}} (\boldsymbol{I}(1 - \boldsymbol{r} \cdot \boldsymbol{r}) + 2(\boldsymbol{r} \otimes \boldsymbol{r} + \boldsymbol{I} \times \boldsymbol{r})) \tag{4}$$

where $\boldsymbol{I}$ is the identity matrix. The reorientation velocity, $\boldsymbol{v}$, can be found through the incremental change in the orientation, $\boldsymbol{r}$, due to crystal lattice spin, and the relation is given by Eq. (5):

$$\boldsymbol{v} = \frac{1}{2}(\boldsymbol{\omega} + (\boldsymbol{\omega} \cdot \boldsymbol{r})\boldsymbol{r} + \boldsymbol{\omega} \times \boldsymbol{r}) \tag{5}$$

To find the spin vector, $\boldsymbol{\omega}$, we define the spin tensor, $\boldsymbol{\Omega}$, as: $\boldsymbol{\Omega} = \dot{\boldsymbol{R}}^{\boldsymbol{e}} \boldsymbol{R}^{\boldsymbol{eT}}$, where $\boldsymbol{R}^{\boldsymbol{e}}$ is computed with the polar decomposition of the elastic deformation gradient, such that $\boldsymbol{F}^{\boldsymbol{e}}$, as $\boldsymbol{F}^{\boldsymbol{e}} = \boldsymbol{R}^{\boldsymbol{e}} \boldsymbol{U}^{\boldsymbol{e}}$. The spin vector, $\boldsymbol{\omega}$, is then defined as $\boldsymbol{\omega} = vect(\boldsymbol{\Omega})$. Here, $vect(\boldsymbol{\Omega})_i = -\Omega_{j,k}$, where $i \neq j$, $i \neq k$, $j \neq k$, and $i, j, k = 1, 2, 3$ $(j < k)$.

After the ODF is calculated at the current time step, the average value of any orientation dependent property, $\chi(\boldsymbol{r}, t)$, can be computed with Eq. (6):

$$< \chi >= \int_{R_t} \chi(\boldsymbol{r}, t) \boldsymbol{A}(\boldsymbol{r}, t) dv_t = \int_{R} \chi(\hat{\boldsymbol{r}}(\boldsymbol{s}, t), t) \boldsymbol{A_0}(\boldsymbol{s}) dv \tag{6}$$

where dv_t is a volume element in the re-oriented domain. The presented model is significantly faster compared to a CPFE model of the microstructure and thus, is feasible to perform a coupled simulation of texture evolution during a forming process. The fundamental region is discretized using an FE mesh as shown in Figure 1. The re-orientation of each node in the fundamental region is computed using an elasto-viscoplastic single crystal model which is described next.

2.2. Elasto-viscoplastic single crystal model

The micro-macro linking approach in this work is similar to the presented by Kumar and Dawson [23] for the crystal constitutive model, and it is explained in more details in Ref. [5]. The classical single-crystal plasticity theory presented previously by Refs. [7, 8, 9, 22, 24, 25, 26, 27, 28, 29], is employed for the ODF model. According to this model, the deformations are large and monotonic, and therefore the elastic effects are ignored. The underlying assumption is that the plastic flow occurs through

slip on prescribed slip systems. The crystal constitutive model is based on the rate-independent single-crystal plasticity model developed by Anand and Kothari [6].

In the rate-independent single crystal model [6]. We first assume that each slip system can be represented with an orthonormal vector pair of the slip direction and slip plane normal, $(\boldsymbol{m^\alpha}, \boldsymbol{n^\alpha})$, respectively. The deformation gradient, $\boldsymbol{F}$, is involved in elastic and plastic components such that $\boldsymbol{F} = \boldsymbol{F^e F^p}$ with $\det(\boldsymbol{F^p}) = 1$. The Green elastic strain, $\boldsymbol{E} = \frac{1}{2}(\boldsymbol{F^{eT} F^e} - \boldsymbol{I})$, is used to model small elastic strains on the unstressed configuration. Next, the conjugate stress is defined in terms of the Cauchy stress, $\boldsymbol{T}$, in the sample reference frame such that $\boldsymbol{T} = \det(\boldsymbol{F^e})(\boldsymbol{F^e})^{-1}\boldsymbol{T}(\boldsymbol{F^e})^{-T}$. The stress constitutive equation is defined as $\bar{\boldsymbol{T}} = \boldsymbol{\mathcal{L}^e}[\boldsymbol{E^e}]$. Here, $\boldsymbol{\mathcal{L}^e}$ is the fourth-order anisotropic elasticity tensor. The evolution of the plastic flow is represented by Eq. (7):

$$\boldsymbol{L^p} = \dot{\boldsymbol{F}}^{\boldsymbol{p}}(\boldsymbol{F^p})^{-1} = \sum_{\alpha} \dot{\gamma}^{\alpha} \boldsymbol{S_0}^{\alpha} \mathrm{sign}(\tau^{\alpha}), \tag{7}$$

where $\boldsymbol{S_0}^{\boldsymbol{\alpha}} = \boldsymbol{m^\alpha} \otimes \boldsymbol{n^\alpha}$ is the Schmid tensor and $\dot{\gamma}^{\alpha}$ is the plastic shearing rate on the slip system, α. The resolved stress on the αth slip system is given by $\boldsymbol{\tau^\alpha} = \bar{\boldsymbol{T}}\dot{\boldsymbol{S}}_{\boldsymbol{0}}^{\boldsymbol{\alpha}}$. The resolved shear stress, $\boldsymbol{\tau^\alpha}$, has the critical value s^α on active slip systems $(\dot{\gamma}^{\alpha} > 0)$. The shear rate is obtained by utilizing a viscoelastic constitutive relation [8] as shown in Eq. (8):

$$\dot{\gamma}^{\alpha} = a_0 \frac{\tau^{\alpha}}{\hat{\tau}} \left| \frac{\tau^{\alpha}}{\hat{\tau}} \right|^{\frac{1}{m-1}}, \tag{8}$$

where m is the rate sensitivity, $\hat{\tau}$ is the slip system hardness, and a_0 is the reference strain rate. The resolved shear stress does not exceed s^α on the inactive systems with $\dot{\gamma}^{\alpha} = 0$. The slip resistance, s^α, is obtained with the hardening law as shown in Eq. (9):

$$\dot{s}^{\alpha}(t) = \sum_{\beta} h^{\alpha\beta}\dot{\gamma}^{\beta}, \quad s^{\alpha}(0) = {s_0}^{\alpha}. \tag{9}$$

More details on the time integration procedure of the constitutive model is given by Anand and Kothari [6]. The microstructural evolution is obtained by computing the reorientation velocity using Eq. (5).

2.3. Forming process simulation

The microstructure is analyzed in this work using the constitutive model which is based on the continuum slip theory. The homogenization is used to derive the overall microstructural response at the macro-scale. In the homogenization approach, it is assumed that the deformation gradient at the macro-scale can be represented through the motion of the exterior microstructure boundary [27]. Next, the homogenized deformation gradient is linked with the deformation of the microstructure using

https://doi.org/10.1016/j.heliyon.2019.e01225

the non-uniform deformations within the microstructure by assuming homogenous deformation for the boundaries of the microstructure. This assumption is preferred over the Taylor hypothesis [22] since the Taylor assumption leads to a stiff upper bound material response.

The macro-scale deformation problem is solved with a Lagrangian formulation. In this problem, a material with the initial configuration is defined as $\boldsymbol{B_0}$. Next, the material is deformed to obtain a new configuration, $\boldsymbol{B_{n+1}}$ at time $t = t_n + 1$. The total deformation gradient $\boldsymbol{F}$ at time $t = t_n + 1$ can be represented with $\boldsymbol{F_n}$ at time $t = t_n$ as $\boldsymbol{F = F_r F_n}$, where $\boldsymbol{F_r}$ is the relative deformation gradient. The equilibrium equation at $t = t_n + 1$ can be expressed in the reference configuration $\boldsymbol{B_n}$ in the absence of body forces as shown in Eq. (10):

$$\nabla_n \cdot < \boldsymbol{P_r} >= 0 \tag{10}$$

where ∇_n denotes the divergence in $\boldsymbol{B_n}$. The averaged Piola-Kirchhoff stress, $< \boldsymbol{P_r} >$, is computed on the unit area of $\boldsymbol{B_n}$ by the average Cauchy stress ($< \boldsymbol{T} >$), which is calculated from ODF averaging equation (Eq. (6)) such that $< \boldsymbol{P_r} >= det\boldsymbol{F_r} < \boldsymbol{T} > \boldsymbol{F_r}^{-T}$. In the current iteration, the solution of the deformation processing problem evolves in an incremental way starting from the initial configuration, $\boldsymbol{B_0}$. Each increment requires the solution of the virtual work equation which is shown in Eq. (11):

$$\int_{\boldsymbol{B_n}} < \boldsymbol{P_r} > \cdot \nabla_n \tilde{\boldsymbol{u}} dV_n = \int_{\boldsymbol{\Gamma_n}} \boldsymbol{t} \cdot \tilde{\boldsymbol{u}} dA_n \tag{11}$$

where the test displacement $\tilde{\boldsymbol{u}}$ is defined over the initial configuration, $\boldsymbol{B_n}$. The implicit traction, $\boldsymbol{t}$, in Eq. (11) arises from the contact between surfaces. An augmented Lagrangian framework, presented in Ref. [5], is used to solve the contact problem. The details regarding the solution for the averaged Piola-Kirchhoff stress can be found in Ref. [5].

The weak form (Eq. (11)) is solved with the finite element method using bilinear quadrilateral elements for the microstructure along with the assumed stress-strain analysis framework. The presented multi-scale modeling and microstructure homogenization techniques have been implemented into an in-house parallel environment in C++ [5] and PetSc parallel toolbox [30]. The multi-scale framework is achieved with modeling macro-points subjected to deformations that are corresponding to processing conditions and transferred to the boundaries of the microstructure using the homogenous boundary assumption.

3. Results & discussion

The presented formulation in the previous section is utilized to achieve the multi-scale modeling framework of Al-Li 2070 alloy. An intermediate step to build the

https://doi.org/10.1016/j.heliyon.2019.e01225

multi-scale model is to find the slip system parameters of the alloy using the available experimental data in Refs. [12, 13]. The used slip system hardening model is given in Eq. (12):

$$h^{\alpha\beta} = [q + (1 - q)\delta^{\alpha\beta}]h^{\beta} \text{ (no sum on } \beta) \tag{12}$$

where q is the latent-hardening ratio (which 1.4 for non-coplanar slip systems), h^{β} is a single slip hardening rate, and $\delta^{\alpha\beta}$ is the Kronecker delta function. The following specific form in Eq. (13) is adopted for the single-slip hardening rate:

$$h^{\beta} = h_o(1 - \frac{s^{\beta}}{s_s})^a \tag{13}$$

where h_o, a, and s_s are slip hardening parameters to be found and they are taken to be identical for all slip systems. The single crystal elastic parameters are taken as: $C_{11} = 106.03$ GPa, $C_{12} = 55.27$ GPa and $C_{44} = 30.97$ GPa [13]. The slip is assumed to occur in the 12 $\{111\} < 110 >$ slip systems in the face-centered cubic (FCC) crystal.

3.1. Computation of multi-scale sensitivities

In this work, the slip system parameters of the Al-Li 2070 alloy are found with a gradient-based optimization scheme which uses the MCSM to compute the sensitivities [5]. The MCSM involves the differentiation of the governing field equations for homogenization with respect to the design variables and development of the weak form for the corresponding sensitivity equations. The technique first calculates the sensitivity of the deformation field within the microstructure and then finds the sensitivity of the homogenized stresses at the macro-scale due to the perturbations of the design variables. The MCSM has been previously employed in Ref. [5] to find the optimum processing parameters (design variables were defined as the process-related parameters). However, in this work, the MCSM is utilized to model the design variables, which are defined as the slip system parameters of Al-Li 2070 alloy. The corresponding perturbation definitions for the slip system parameters are given in Eq. (14):

$$\begin{aligned} \overline{s_0^{\alpha}} &= s_0^{\alpha} + \delta_{s_0{}^{\alpha}} \\ \overline{h} &= h + \delta_h \\ \overline{s_s} &= s_s + \delta_{s_s} \\ \overline{a} &= a + \delta_a \end{aligned} \tag{14}$$

where $\overline{s_0^{\alpha}}$, $\overline{h}$, $\overline{s_s}$, and $\overline{a}$ show the perturbed values of the slip system parameters. The gradient of the specific form of the single-slip hardening rate can be then found as in Eq. (15):

 https://doi.org/10.1016/j.heliyon.2019.e01225

$$\nabla h^{\beta} = [\frac{\partial h^{\beta}}{\partial h_0}, \frac{\partial h^{\beta}}{\partial s_s}, \frac{\partial h^{\beta}}{\partial a}]^T \tag{15}$$

where the corresponding partial derivatives can be calculated as given in Eq. (16):

$$\begin{aligned} \frac{\partial h^{\beta}}{\partial h_0} &= (1 - \frac{s^{\beta}}{s_s})^a \\ \frac{\partial h^{\beta}}{\partial s_s} &= a h_0^2 \frac{s^{\beta}}{s_s^2} (1 - \frac{s^{\beta}}{s_s})^{a-1} \\ \frac{\partial h^{\beta}}{\partial a} &= c_1 h^{\beta} \end{aligned} \tag{16}$$

where c_1 can be calculated as $c_1 = ln(h_0(1 - \frac{s^{\beta}}{s_s}))$. The perturbations are also propagated to the constitutive relations (presented in Section 2.2) such as given in Eq. (17):

$$\overline{h^{\alpha\beta}} = [q + (1 - q)\delta^{\alpha\beta}]\overline{h^{\beta}} \tag{17}$$

The propagation of the perturbations to the other constitutive parameters can be found similarly. For example, since $\dot{s}^{\alpha}$ is a function of $h^{\alpha\beta}$, ($\dot{s}^{\alpha} = f(h^{\alpha\beta})$ as given in Eq. (9)) the perturbed equation will have the form: $\overline{\dot{s}^{\alpha}} = f(\overline{h^{\alpha\beta}})$. The propagation to the constitutive model parameters will follow the path: $\overline{s^{\alpha}} \rightarrow \overline{\tau^{\alpha}} \rightarrow \overline{\boldsymbol{T}} \rightarrow \overline{\boldsymbol{F}^p}, \overline{\boldsymbol{F}^e}, \overline{\boldsymbol{F}}, \overline{\boldsymbol{E}}, \overline{\boldsymbol{L}^p}$. The presented version of MCSM utilizes the perturbations of the slip system parameters to the constitutive model for the first time since the model was previously adapted to compute the perturbations of the processing parameters [5]. However, the propagation of the perturbations within the constitutive model parameters are discussed in details in Ref. [5], and it is not repeated here for brevity. The interest in this problem is to compute how perturbations on the slip system variables affect the micro-fields, mainly the stresses within the microstructure. According to the MCSM [5], the multi-scale sensitivity linking is defined as follows: First, the sensitivity of the averaged deformation gradient at a material point is computed with the aforementioned procedure. The sensitivity of the averaged deformation gradient at a material point is assumed to be the same as the sensitivity of the deformation gradient on the boundary of the underlying microstructure in the reference frame. Next, the equilibrium equation for the microstructure is considered and differentiated. To find the virtual work equation, the sensitivity equilibrium equation is posed in weak form using the sensitivity equilibrium relation shown in Eqs. (18) and (19).

$$\overline{\nabla_n \cdot \boldsymbol{P_r}} = 0 \tag{18}$$

where the weak form can be represented as:

$$\int_{B_n} \overline{\boldsymbol{P_r}} \cdot \nabla_n \tilde{\boldsymbol{u}} dV_n = 0 \tag{19}$$

Table 1. Crystal plasticity parameters calibrated for compression Al-Li alloy sample.

Parameter	Value
s_0	145.6 MPa
h_0	67.4 MPa
s_s	292.2 MPa
a	2.25

Using the sensitivity constitutive relation, Eq. (19) is solved for the stress sensitivities in the microstructure due to the perturbations in the slip system parameters. Next, the sensitivity of the PK-1 stress is converted to the sensitivity of the homogenized Cauchy stress. The sensitivity of the equivalent stress can be found as in Eq. (20):

$$\overline{\sigma_{\bar{eff}}} = \frac{3}{2\sigma_{\bar{eff}}} \bar{\boldsymbol{T}}' \overline{\bar{\boldsymbol{T}}}' \tag{20}$$

3.2. Optimization of slip system parameters

The goal of slip system parameters optimization is to match the computed equivalent stresses over the deformation history of the material as a function of the slip system parameters, s_0, h_0, s_s, and a. The experimental data presented in Refs. [12, 13] is used to compare the simulated compression stress-strain curve and microstructural textures. The objective function of the slip system parameters determination problem is defined as the minimization of the difference between the experimental (presented in Refs. [12, 13]) and computed compression stress-strain curves to calibrate the CP model using Sequential Quadratic Programming (SQP) algorithm. The multi-scale simulation is performed for a plane strain compression mode using a randomly oriented initial texture assumption. The experimental initial texturing of the alloy was found to have variations around a random texture because of the processing uncertainties. This also means that the average values of the texture parameters (ODFs) demonstrate a random texture representation with a known experimental stress-strain test data. Therefore, in this work, we neglected the small variations and assumed that the initial experimental texture is random, and we used the same assumption in the simulations. The constant ODF value of the random texture is taken as $A(r, 0) = 2.435$. The CP model calibration study finds the following optimum slip system parameters shown in Table 1. The simulations are compared to the experimental data up to a strain of 60 %. The given parameters in Table 1 lead to the compression stress-strain curve that is compared to the presented experimental data (Refs. [12, 13]) in Figure 2.

After identification of the slip system parameters, the multi-scale simulation is performed for Al-Li 2070 alloy to compute the textures which are then compared to the experimentally available texture data in Ref. [12]. For the experimental textures,

 https://doi.org/10.1016/j.heliyon.2019.e01225

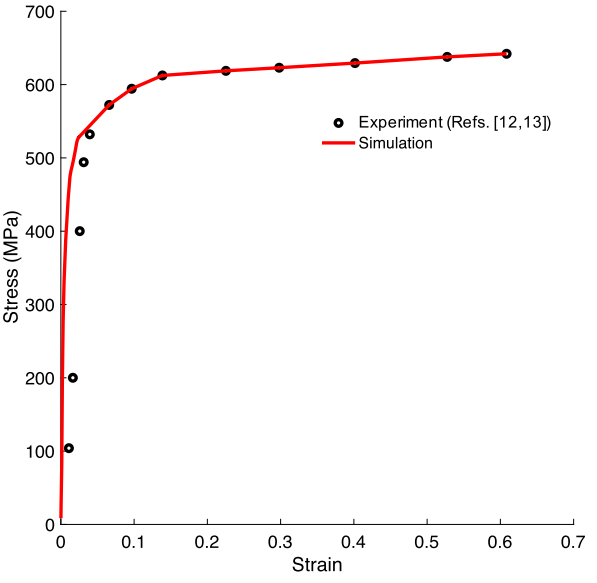

Figure 2. Compression stress-strain response of the ODF model compared to experimental data.

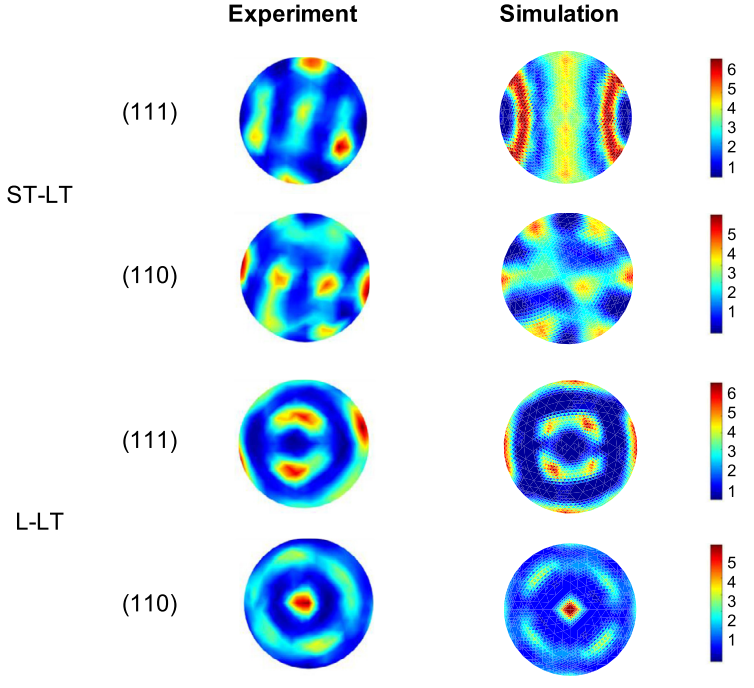

Figure 3. Experimental and simulated pole figures after compression (strain at 60%).

we use the presented data in Ref. [12] for a material that was received as a H-forged specimen with the thickness of 10.16 cm. Figure 3 shows the texture predictions for the compression process and the corresponding experimental measurements. The (111) and (110) pole figures for both ST-LT and the L-LT faces are compared in Figure 3. According to the plots in Figure 3, the results compare favorably such

 https://doi.org/10.1016/j.heliyon.2019.e01225

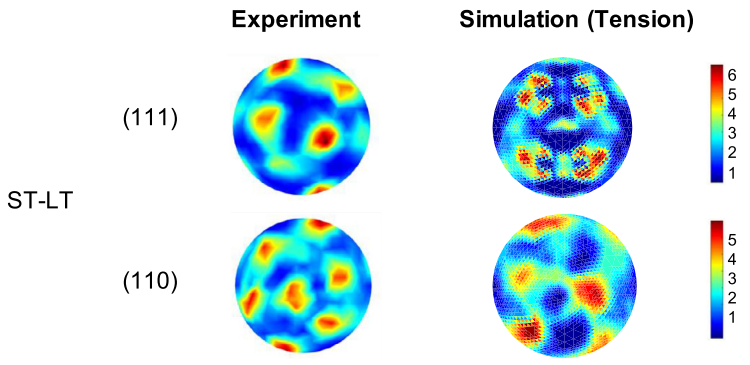

Figure 4. Measured and simulated pole figures after tensile deformation at a strain of 50%.

that all predominant texture components from the experiments are identified in computations.

For texture comparisons, a multi-scale simulation for tensile deformation is also performed. Figure 4 shows the (111) and (110) pole figures on the ST-LT surface of the material during a tensile test at a strain of 50% [12]. The predominant experimental texture components (Ref. [12]) are also well captured in the tensile test. However, as shown in both Figures 3 and 4, the location of the predominant texture modes is rotated by a very small angle compared to the location of the ideal components. The reason for having a rotation on the results is that the multi-scale simulations are performed for ideal compression and tension modes to predict the textures. However, the specimen in the experiments might have deformed asymmetrically because of the shear associated with barreling, necking, or shear banding. The small variations in the experimental data are usual and considered as a natural variation (or aleatoric uncertainty), and have been analyzed in details in the previous work of the authors [17, 18]. However, in this work, we neglect the effects of experimental uncertainties in the simulations.

The multi-scale study shown here considers upset forging of a cylindrical billet (of Al-Li 2070 alloy) between parallel flat dies. The model uses 145 ODF values at the micro-scale at each integration point in an FE macro-scale mesh. The simulation is performed by assuming a rigid die with a contact friction of 0.1 at the top surface. The bottom surface is pushed up against the die using displacement boundary conditions. The initial cylindrical billet has a 2 mm diameter and 3 mm height. The multi-scale simulation leads to the prediction of the texture evolution at every material point in the macro-specimen. Figure 5 shows the textures predicted at selected locations at engineering strain levels of 10%, 40% and 70%. The distribution of the von Mises stresses at the macroscopic level is also shown in Figure 5. Although this particular simulation involves relatively a small number of texture components, the presented multi-scale scheme is capable of simulating a larger number of ODFs. However, the increase in the micro-scale size leads to a corresponding increase in the simulation

 https://doi.org/10.1016/j.heliyon.2019.e01225

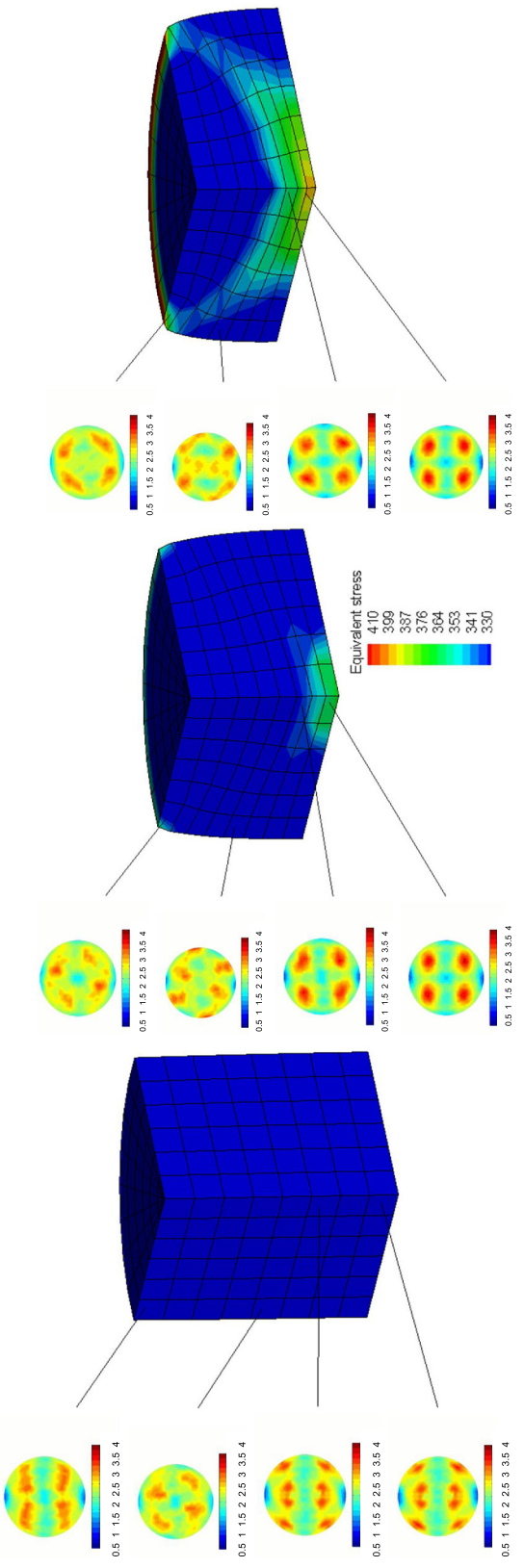

Figure 5. Figure showing the distribution of the von Mises stresses across the FE mesh throughout the simulation, with the left pane depicting the stress at the first time step, the middle pane at the median time step, and the right pane at the final time step. The pole figure density of the (111) textures predicted (color bar variable) at specific locations in the FE mesh are inset to each pane.

 https://doi.org/10.1016/j.heliyon.2019.e01225

time. To speed up the solution of the multi-scale problem, Message Passing Interface (MPI) is used and linked to the parallel toolbox PetSc [30] for parallelization and solution of linear systems. In particular, for the solution of linear systems, a GMRES solver is used from the PetSc toolbox. The computational time for the presented multi-scale simulation is around 86 hours on an 8 core machine.

4. Conclusions

We address a fully-coupled multi-scale modeling for lightweight Al-Li 2070 alloy that allows the prediction of texture evolution during industrial forming processes. The modeling effort starts from the micro-scale using an Orientation Distribution Function (ODF) to represent the microstructure. In the multi-scale framework, the deformation at the macro-scale element integration points is passed to the micro-scale model and the stress tensor at the micro-scale (and the tangent moduli) is passed back to the macro-scale model. Using this multi-scale model with an elasto-plastic single crystal constitutive model, we perform multi-scale simulations for Al-Li 2070 alloy by utilizing the Multi-Scale Continuum Sensitivity Method (MCSM) and a gradient-based optimization solver to identify the optimum slip system parameters. The multi-scale simulations are achieved for both tension and compression, and all simulation results lead to accurate predictions for the texture evolution when compared to the available experimental data as shown in Figures 2, 3 and 4. The multi-scale simulations are performed by modeling 145 ODF values at each material point. The accuracy of the texture predictions can be further improved in the future by increasing the micro-scale finite element mesh density. However, due to the computational time requirements of the multi-scale materials simulations, surrogate models may also be utilized as a future work to perform the high-fidelity multi-scale material simulations. Another future area can be the development of a modeling capability to achieve the multi-scale design of multi-phase materials since the current ODF based methodology is adapted to model single phase alloys as presented in this work.

Declarations

Author contribution statement

Pinar Acar: Conceived and designed the analysis; Analyzed and interpreted the data; Contributed analysis tools or data; Wrote the paper.

Funding statement

This work was supported by Virginia Polytechnic Institute and State University.

Competing interest statement

The authors declare no conflict of interest.

Additional information

No additional information is available for this paper.

Acknowledgements

The author would like to thank to Prof. Veera Sundararaghavan from University of Michigan for his valuable suggestions in multi-scale modeling.

References

[1] R.J. Rioja, J. Liu, The evolution of Al-Li base products for aerospace and space applications, Metall. Mater. Trans. A, Phys. Metall. Mater. Sci. 43A (9) (2012) 3325–3337.

[2] T. Dursun, C. Soutis, Recent developments in advanced aircraft aluminum alloys, Mater. Des. 56 (2014) 862–871.

[3] A.A. Gokhale, N.E. Prasad, Aluminum-Lithium Alloys: Processing, Properties, and Applications, Butterworth-Heinemann, 2013.

[4] H. Garmestani, S.R. Kalidindi, L. Williams, C.M. Bacaltchuk, C. Fountain, E.W. Lee, O.S. Es-Said, Modeling the evolution of anisotropy in Al-Li alloys: application to Al-Li 2090-T8E41, Int. J. Plast. 18 (10) (2002) 1373–1393.

[5] V. Sundararaghavan, N. Zabaras, A multi-length scale sensitivity analysis for the control of texture-dependent properties in deformation processing, Int. J. Plast. 24 (9) (2008) 1581–1605.

[6] L. Anand, M. Kothari, A computational procedure for rate-independent crystal plasticity, J. Mech. Phys. Solids 44 (4) (1996) 525–558.

[7] R.J. Asaro, Micromechanics of crystals and polycrystals, Adv. Appl. Mech. 23 (1983) 1–115.

[8] R.J. Asaro, A. Needleman, Texture development and strain hardening in rate dependent polycrystals, Acta Metall. 33 (1985) 923–953.

[9] C.A. Bronkhorst, S.R. Kalidindi, L. Anand, Polycrystalline plasticity and the evolution of crystallographic texture in FCC metals, Philos. Trans. R. Soc. Lond. A 341 (1992) 443–477.

 https://doi.org/10.1016/j.heliyon.2019.e01225

[10] L.T. Li, Y.C. Lin, L. Li, L.-M. Shen, D.-X. Wen, Three-dimensional crystal plasticity finite element simulation of hot compressive deformation behaviors of 7075 Al alloy, J. Mater. Eng. Perform. 24 (3) (2015) 1294–1304.

[11] A. Staroselsky, L. Anand, A constitutive model for hcp materials deforming by slip and twinning: application to magnesium alloy AZ31B, Int. J. Plast. 19 (10) (2003) 1843–1864.

[12] L.B. Borkowski, J.A. Sharon, A. Staroselsky, An elastic-visco-plastic deformation model of Al-Li with application to forging, Int. J. Comput. Methods Exp. Meas. 6 (4) (2018) 635–646.

[13] L.B. Borkowski, J.A. Sharon, A. Staroselsky, In situ micromechanical testing for single crystal property characterization, Metall. Mater. Trans. A 49 (12) (2018) 6022–6033.

[14] P. Acar, V. Sundararaghavan, Utilization of a linear solver for multiscale design and optimization of microstructures, AIAA J. 54 (5) (2016) 1751–1759.

[15] P. Acar, V. Sundararaghavan, Linear solution scheme for microstructure design with process constraints, AIAA J. 54 (12) (2016) 4022–4031.

[16] P. Acar, V. Sundararaghavan, Uncertainty quantification of microstructural properties due to experimental variations, AIAA J. 55 (8) (2017) 2824–2832.

[17] P. Acar, V. Sundararaghavan, Uncertainty quantification of microstructural properties due to variability in measured pole figures, Acta Mater. 124 (2017) 100–108.

[18] P. Acar, S. Srivastava, V. Sundararaghavan, Stochastic design optimization of microstructures with utilization of a linear solver, AIAA J. 55 (9) (2017) 3161–3168.

[19] V. Sundararaghavan, A. Kumar, Probabilistic modeling of microstructure evolution using finite element representation of statistical correlation functions, Int. J. Plast. 30–31 (2012) 62–80.

[20] A. Kumar, P.R. Dawson, Modeling crystallographic texture evolution with finite elements over neo-Eulerian orientation spaces, Comput. Methods Appl. Mech. Eng. 153 (1997) 259–302.

[21] S. Sun, V. Sundararaghavan, A probabilistic crystal plasticity model for modeling grain shape effects based on slip geometry, Acta Mater. 60 (2012) 5233–5244.

[22] G. Taylor, Plastic strain in metals, J. Inst. Met. 62 (1938) 307–324.

[23] A. Kumar, P.R. Dawson, Computational modeling of F.C.C. deformation textures over Rodrigues' space, Acta Mater. 48 (10) (2000) 2719–2736.

 https://doi.org/10.1016/j.heliyon.2019.e01225

[24] J. Mandel, Generalization de la theorie de la plasticite de W.T Koiter, Int. J. Solids Struct. 1 (1965) 273–295.

[25] J.R. Rice, Inelastic constitutive relations for solids: an internal variable theory and its application to metal plasticity, J. Mech. Phys. Solids 19 (1971) 433–455.

[26] J. Mandel, Plasticite Classique et Viscoplasticite, CISM Courses and Lectures, vol. 97, Springer, Berlin, 1972.

[27] R. Hill, Continuum micro-mechanics of elastoplastic polycrystals, J. Mech. Phys. Solids 13 (1965) 89–101.

[28] C. Teodosiu, F. Sidoroff, A theory of finite elastoviscoplasticity of single crystals, Int. J. Eng. Sci. 14 (1976) 165–176.

[29] A.M. Cuitino, M. Ortiz, Computational modeling of single crystals, Model. Simul. Mater. Sci. Eng. 1 (1992) 225–263.

[30] S. Balay, K. Buschelman, V. Eijkhout, W.D. Gropp, D. Kaushik, M.G. Knepley, L.C. McInnes, B.F. Smith, H. Zhang, PETSc Users Manual ANL-95/11 - Revision 2.1.5, Argonne National Laboratory, 2004.

 https://doi.org/10.1016/j.heliyon.2019.e01225